

# Theory of Electron Spin Resonance Spectroscopy in Scanning Tunneling Microscopy

Lyuzhou Ye,<sup>1</sup> Xiao Zheng,<sup>2,\*</sup> and Xin Xu<sup>2,3,†</sup>

<sup>1</sup>*Hefei National Research Center for Interdisciplinary Sciences at the Microscale  
& Synergetic Innovation Center of Quantum Information and Quantum Physics,  
University of Science and Technology of China, Hefei, Anhui 230026, P. R. China*

<sup>2</sup>*Department of Chemistry, Fudan University, Shanghai, 200433, P. R. China*

<sup>3</sup>*Hefei National Laboratory, Hefei 230088, P. R. China*

(Dated: Updated on February 7, 2024)

The integration of scanning tunneling microscopy (STM) and electron spin resonance (ESR) spectroscopy has emerged as a powerful and innovative tool for discerning spin excitations and spin-spin interactions within atoms and molecules adsorbed on surfaces. However, the origin of the STM-ESR signal and the underlying mechanisms that govern the essential features of the measured spectra have remained elusive, thereby significantly impeding the future development of the STM-ESR approach. Here, we construct a model to carry out precise numerical simulations of STM-ESR spectra for a single hydrogenated Ti adatom and a hydrogenated Ti dimer, achieving excellent agreement with experimental observations. We further develop an analytic theory that elucidates the fundamental origin of the signal as well as the essential features in the measured spectra. These new theoretical developments establish a solid foundation for the on-demand detection and manipulation of atomic-scale spin states, with promising implications for cutting-edge applications in spin sensing, quantum information, and quantum computing.

**Introduction.** The precise measurement and control of spin states of single atoms and molecules [1–3] serve as the foundation for cutting-edge applications in spintronics [4–6], quantum sensing [7, 8], quantum information [9, 10], and quantum computing [11, 12]. Over the last decade, the synergistic integration of electron spin resonance (ESR) technique with scanning tunneling microscopy (STM) has fundamentally transformed the ability to detect and analyze spin states in atoms and molecules adsorbed on surfaces, offering unprecedented spatial and energy resolution [7–26]. The STM-ESR spectroscopy provides profound insights into spin-related properties of single atoms and molecules, including spin-state transitions and spin couplings between magnetic centers. Recent strides made in STM-ESR have enabled coherent control over the temporal evolution of atomic spin states [25, 26], leading to the establishment of an atomic-scale multi-qubit platform [27], further advancing the frontier of quantum technologies.

Despite the remarkable success of the STM-ESR technique, there is a persistent ambiguity regarding the origin of the STM-ESR signal [28, 29]. Unlike conventional ESR experiments that employs alternating magnetic fields to probe macroscopic samples [30], the STM-ESR technique utilizes an applied alternating voltage as the driving source. This raises the intriguing question: How exactly does the applied alternating voltage lead to the detected spin resonance signal? Various mechanisms, including spin-phonon-like coupling [31], current-induced spin-transfer torque [32], molecular piezoelectric response [14, 21, 33], and modulation of electron tunnel barrier [34, 35], have been proposed. However, these hy-

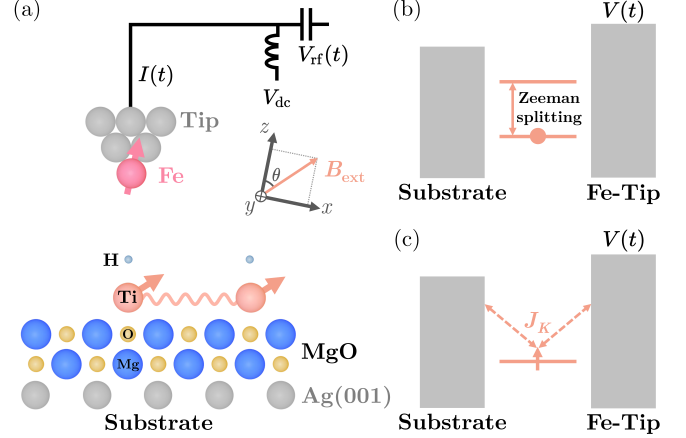


FIG. 1. (a) Sketch of the experimental setup, where the STM tip with an Fe atom at its apex is utilized to probe spin-1/2 hydrogenated Ti adatoms. The substrate consists of a bilayer MgO grown on Ag(001). The spin moment of Fe atom is along  $\hat{z}$ . An external magnetic field  $B_{ext}$  is applied in the  $xz$ -plane, with the angle  $\theta$  determining its direction relative to  $\hat{z}$ . A bias voltage, composed of  $V_{dc}$  and  $V_{rf}(t)$ , is applied to the tip, resulting in the time-varying electric current  $I(t)$ . (b) Illustration of the AIM, and (c) illustration of the Kondo model, where  $J_K$  denotes the Kondo exchange interaction.

potheses do not fully account for the key experimental features observed. Additionally, numerical simulations comprehensively reproducing experimental results have remained out of reach. These unresolved theoretical challenges significantly impede a complete understanding and future advancement of the STM-ESR approach.

This paper aims to tackle these challenges by constructing a model to carry out precise numerical simulations of STM-ESR spectra that align with experimen-

\* xzheng@fudan.edu.cn

† xxchem@fudan.edu.cn

tal findings. More importantly, taking the perspective of many-body open quantum system, a fundamental theory is established here that clarifies the origin of the signal and explicates the essential characteristics observed in the measured spectra.

*Modeling the experimental setup.* Figure 1(a) illustrates the setup of the STM-ESR experiment. The ESR signal is attained as the direct current (dc) component of electric current driven by a time-dependent bias voltage  $V(t) = V_{\text{dc}} + V_{\text{rf}} \sin(\omega_{\text{rf}} t)$  [16, 25, 26], where  $V_{\text{dc}}$  and  $V_{\text{rf}}(t)$  denote a constant dc voltage and a continuous-wave radio-frequency (rf) voltage, respectively.

We adopt the Anderson impurity model (AIM) to represent the STM junction. The total Hamiltonian consists of three parts, i.e.,  $H_{\text{T}} = H_{\text{imp}} + H_{\text{res}} + H_{\text{coup}}$ . Here, the impurity Hamiltonian  $H_{\text{imp}}$  describes the magnetic orbitals of the surface-adsorbed atom or molecule. In the case of a single hydrogenated Ti adatom, the impurity represents a singly occupied localized orbital described by

$$H_{\text{imp}} = \epsilon(\hat{n}_{\uparrow} + \hat{n}_{\downarrow}) + U\hat{n}_{\uparrow}\hat{n}_{\downarrow} + H_{\text{Zeeman}}, \quad (1)$$

where  $\hat{n}_{\sigma}$  is the spin- $\sigma$  electron number operator, and  $\epsilon$  and  $U$  are the orbital energy and the electron-electron interaction energy, respectively.  $H_{\text{Zeeman}} = g\mu_B \mathbf{B}_{\text{ext}} \cdot \hat{\mathbf{S}}$ , where  $g$  is the electron Zeeman factor,  $\mu_B$  is the Bohr magneton,  $\hat{\mathbf{S}}$  is the local spin operator, and  $\mathbf{B}_{\text{ext}}$  is the external magnetic field that includes the field generated by the permanent spin moment of Fe atom at the tip apex.

In the AIM,  $H_{\text{res}}$  represents the tip and substrate that are regarded as non-interacting electron reservoirs (res), while  $H_{\text{coup}}$  describes the impurity-reservoir couplings (coup). Since the reservoirs follow Gaussian statistics, their impact on the impurity is fully captured by the hybridization functions,  $\Gamma_{\alpha\sigma}(\omega) = \Gamma_{\alpha\sigma} D_{\alpha}(\omega)$ , where  $\Gamma_{\alpha\sigma}$  and  $D_{\alpha}(\omega)$  represent the hybridization strength and dimensionless density of states of  $\alpha$ -reservoir ( $\alpha = t, s$ ), respectively. In the following,  $t$  and  $s$  will be used as the subscripts to represent the tip and substrate, respectively. The tip spin polarization is oriented in the  $\hat{z}$  direction, and its extent is quantified by  $\chi$ , defined as  $\chi \equiv (\Gamma_{t\uparrow} - \Gamma_{t\downarrow}) / \Gamma_t$ , with  $\Gamma_t = \Gamma_{t\uparrow} + \Gamma_{t\downarrow}$ . Further details can be found in the Supplementary Material (SM) [36].

A clear characterization of the role played by the applied voltage in the spin signal generation is fundamentally important for unraveling the underlying mechanisms of STM-ESR. In our model, the voltage primarily modulates the electrochemical potential of the tip, as shown in Fig. 1(b), without altering the electron tunneling barrier itself [34, 35]. This voltage drives the quantum dynamics of the STM junction, encompassing both charge and spin degrees of freedom. It is noteworthy that the energy scale associated with spin dynamics (approximately  $\sim 10$  meV) is significantly lower compared to that of charge dynamics ( $\sim 1$  eV). By leveraging the Schrieffer-Wolff transformation [37], we can formally distinguish between these two disparate energy scales. Con-

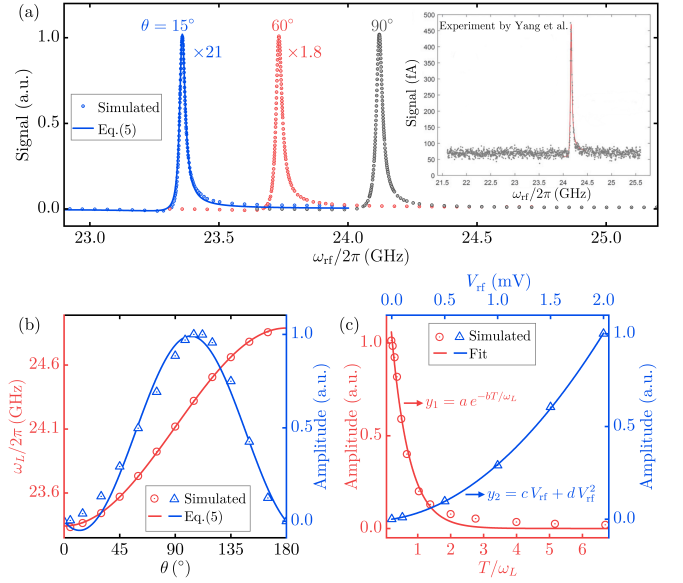


FIG. 2. (a) Simulated STM-ESR spectra (circles) of a single hydrogenated Ti adatom at different angles  $\theta$  [see Fig. 1(a) for definition of  $\theta$ ], with the analytic expression of Eq. (5) at  $\theta = 15^\circ$  (line) shown for comparison. All peaks are normalized to the same height. The inset displays the experimental result obtained by Yang et al. [16]. (b) Variation of the resonance frequency  $\omega_L$  (left axis) and amplitude (right axis) with respect to  $\theta$ , where the lines represent the predictions by the analytic theory using Eq. (5). (c) Variation of the signal amplitude with respect to temperature  $T$  (left and bottom axes) and  $V_{\text{rf}}$  (right and top axes) at  $\theta = 90^\circ$ . The data are fitted to an exponentially decaying function  $y_1(T/\omega_L)$  and nonlinear function  $y_2(V_{\text{rf}})$ , respectively. Other parameters adopted are:  $|\mathbf{B}_{\text{ext}}| = 0.86$  T,  $\epsilon = -6$  meV,  $\Gamma_s = 0.2$  meV,  $\Gamma_t = 0.01$  meV,  $\chi = 0.9$  and  $V_{\text{dc}} = 0.4$  mV. Specifically,  $T = 1.2$  K and  $V_{\text{rf}} = 0.2$  mV are used in (a) and (b).

sequently, we arrive at a spin-polarized Kondo model that focuses specifically on the spin degrees of freedom, as illustrated in Fig. 1(c).

*Numerical simulation of STM-ESR spectra.* We perform precise simulations on the constructed AIM by employing the numerically exact hierarchical equations of motion (HEOM) method implemented in the HEOM-QUICK2 program [38–43]. The STM-ESR spectra are acquired by directly calculating and averaging the time-dependent electric current  $I(t)$  in response to the applied alternating voltage at different frequencies  $\omega_{\text{rf}}$ .

The substantial disparity in energy scales between charge and spin dynamics presents a significant hurdle for the numerical simulations. Accurate time propagation of the HEOM necessitates a very small time step, resulting in computationally intensive simulations, particularly when extracting the dc component of the electric current. To tackle this difficulty, we consistently scale down the energetic parameters pertaining to charge-state excitations, such as orbital energies and voltage amplitudes, while preserving the distinct separation between

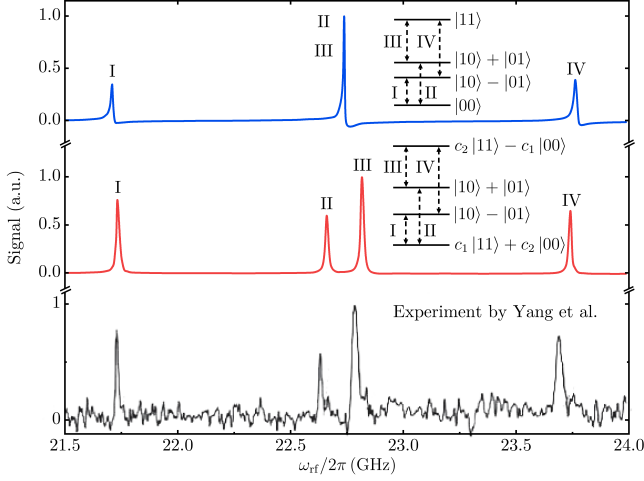


FIG. 3. Simulated STM-ESR spectra of a hydrogenated Ti dimer with  $D = 0$  (upper panel) and  $D = 0.105$  GHz (middle panel), where  $D$  indicates the magnitude of dipolar coupling. The insets depict the lowest spin-states of the hydrogenated Ti dimer, where 0 (1) indicates that the local spin aligns parallel (antiparallel) to  $\mathbf{B}_{\text{ext}}$ . The lower panel presents experimental data extracted from Ref. [16]. Other parameters adopted are  $\epsilon = -6$  meV,  $\Gamma_{s1} = \Gamma_{s2} = 0.04$  meV,  $\Gamma_{t1\uparrow} = 9.5 \times 10^{-3}$  meV,  $\Gamma_{t1\downarrow} = 5 \times 10^{-4}$  meV,  $\Gamma_{t2\uparrow} = \Gamma_{t2\downarrow} = 0$ ,  $V_{\text{dc}} = 0.4$  mV,  $V_{\text{rf}} = 0.2$  mV,  $\theta = 90^\circ$ ,  $|\mathbf{B}_{\text{ext}}| = 0.81$  T,  $J = 1.03$  GHz, and  $T = 1.2$  K.

charge and spin energy scales. Other energetic parameters, such as temperature, Zeeman energy, and hybridization strengths, are carefully chosen to match the experimental conditions [16, 36].

Figure 2(a) displays the simulated STM-ESR spectra of a single hydrogenated Ti adatom, featuring a resonance peak at the frequency  $\omega_L$ , which corresponds to the Zeeman energy. The peak exhibits a somewhat asymmetric lineshape, closely resembling the experimentally measured spectrum depicted in the inset. Moreover, the simulated results reproduce several important features observed in experiments: (i) The peak position and amplitude of the simulated spectra vary prominently with  $\theta$  [see Fig. 1(a) for the definition of  $\theta$ ], as depicted in Fig. 2(b) [44]. Notably, the peak vanishes when  $\mathbf{B}_{\text{ext}}$  aligns parallel to the direction of tip spin polarization at  $\theta = 0$  or  $180^\circ$ . (ii) As demonstrated in Fig. 2(c), the signal amplitude undergoes an exponential decay with increasing temperature  $T$  [45], and exhibits a nonlinear dependence on  $V_{\text{rf}}$  in the low-bias regime [18].

STM-ESR offers a distinct advantage in probing extremely weak spin-spin couplings ( $< 1$  GHz). To demonstrate this capability, we simulate the STM-ESR spectra of a hydrogenated Ti dimer. In experimental settings, the magnitudes of the exchange ( $J$ ) and dipolar ( $D$ ) couplings depend sensitively on the relative distance and orientation of the two spins. These factors can be precisely manipulated by using the tip as a mechanical tweezer [8, 16, 17]. In our simulation, the Fe-

tip exclusively couples to the local spin at one hydrogenated Ti adatom. The couplings between the two local spins are described by the Hamiltonian,  $H_{\text{spin-spin}} = J\hat{\mathbf{S}}_1 \cdot \hat{\mathbf{S}}_2 + D(3\hat{S}_1^z\hat{S}_2^z - \hat{\mathbf{S}}_1 \cdot \hat{\mathbf{S}}_2)$ , which constitutes an additional contribution to  $H_{\text{imp}}$ .

Figure 3 depicts the simulated STM-ESR spectra alongside the experimental result [16]. The resonance peaks are attributed to transitions between the lowest spin-states. In the insets, we observe that a nonzero  $D$  alters the eigenstates of  $H_{\text{imp}}$ , causing the central peak (upper panel) to split into two (middle panel). Remarkably, the simulated spectrum obtained with a finite  $D$  exhibits excellent agreement with the experimental result (lower panel) [16].

The remarkable consistency between the numerical simulations and experimental observations, as evidenced in Figs. 2 and 3, substantially justifies our construction and utilization of the AIM. Our approach, which considers the bias voltage as a modulation of the tip's electrochemical potential has thus been unequivocally confirmed. Despite this numerical validation, the physical origin of the spin resonance signal remains unclear, necessitating further elucidation to comprehend fundamentally the significant characteristics depicted in Fig. 2. We now introduce an analytic theory aimed at addressing this basic need.

*Analytic STM-ESR theory.* Consider a single adatom with a local spin of  $S = 1/2$  [16, 25, 26]. The Schrieffer-Wolff transformation [37] in the large- $U$  limit yields a Zeeman Hamiltonian,  $H_{\text{spin}} = H_{\text{Zeeman}}$ , describing the local spin [36]. In the Kondo model, the local spin interacts with the reservoirs through spin-exchange couplings given by  $H_{\text{int}} = H_{ss} + H_{tt} + H_{st} + H_{ts}$ , where

$$H_{\alpha\alpha'} = \sum_{ikk'\sigma\sigma'} J_{\alpha\alpha'kk'\sigma\sigma'} \hat{S}_{\alpha\alpha'kk'\sigma\sigma'}^i \hat{S}^{i\dagger}. \quad (2)$$

Here,  $i = \{+, -, z\}$ ,  $J_{\alpha\alpha'kk'\sigma\sigma'}$  is the Kondo exchange coupling strength, and  $\hat{S}_{\alpha\alpha'kk'\sigma\sigma'}^i \equiv \hat{d}_{\alpha k\sigma}^\dagger \tau_{\sigma\sigma'}^i \hat{d}_{\alpha'k'\sigma'}$ , with  $\hat{d}_{\alpha k\sigma}^\dagger$  ( $\hat{d}_{\alpha k\sigma}$ ) denoting the creation (annihilation) operator of  $\alpha$ -reservoir and  $\tau^i$  the Pauli matrix.  $H_{\alpha\alpha'}$  represents the transition between reservoir states  $|\alpha k\sigma\rangle$  and  $|\alpha'k'\sigma'\rangle$  mediated by the localized atomic orbital. Specifically,  $H_{ss}$  and  $H_{tt}$  result in the Kondo screening of the local spin by conduction electrons in the reservoirs, while  $H_{st}$  and  $H_{ts}$  describe electron transport between the substrate and tip through electron co-tunneling events. It has to be this electron transport that gives rise to an electric current, which encompasses the STM-ESR signal.

Notably,  $H_{tt}$  exclusively contributes to the mean-field influence of  $H_{\text{int}}$ , i.e.,  $\langle H_{\text{int}}(t) \rangle_{\text{res}} = \langle H_{tt}(t) \rangle_{\text{res}} = g\mu_B B_{\text{tip}}^{\text{eff}}(t) \hat{S}^z$ , where  $\langle \dots \rangle_{\text{res}}$  denotes the trace over all the reservoir states. Consequently, the averaged effect of the spin-polarized tip on the local spin can be captured by an *effective* time-dependent magnetic field along  $\hat{z}$ ,

$$B_{\text{tip}}^{\text{eff}}(t) = \frac{1}{g\mu_B} \sum_k (J_{ttkk\uparrow\uparrow} - J_{ttkk\downarrow\downarrow}) f_\beta(\epsilon_{tk})$$

$$\begin{aligned}
&= \frac{\chi \Gamma_t}{\pi g \mu_B} \int \frac{D_t(\omega) f_\beta(\omega)}{\omega - V_{dc} - V_{rf}(t) - \epsilon} d\omega \\
&\simeq B_0 + B_1 \sin(\omega_{rf} t). \quad (3)
\end{aligned}$$

Here,  $\epsilon_{tk}$  refers to the electron energy in the  $k$ th band of the tip,  $f_\beta(\omega)$  is the Fermi function with  $\beta = 1/T$  denoting the inverse temperature, and we have set  $\hbar = k_B = e = 1$  for brevity. The  $B_{\text{tip}}^{\text{eff}}(t)$  field acts locally on a single spin, offering thus a powerful local probe with atomic-scale spatial resolution for detecting and manipulating intricate spin dynamics.

We can reorganize the Hamiltonian of the local spin and spin-reservoir couplings as follows:  $H'_{\text{spin}}(t) = H_{\text{spin}} + \langle H_{\text{int}}(t) \rangle_{\text{res}} = H'_{\text{Zeeman}} + H_{\text{Drive}}(t)$  and  $H'_{\text{int}}(t) = H_{\text{int}}(t) - \langle H_{\text{int}}(t) \rangle_{\text{res}}$ . Here,  $H'_{\text{Zeeman}} = H_{\text{spin}} + g\mu_B B_0 \hat{S}^z$  results in a renormalized Zeeman splitting, given by  $\omega_L \simeq g\mu_B(|\mathbf{B}_{\text{ext}}| + B_0 \cos \theta)$ ; and  $H_{\text{Drive}}(t) = g\mu_B B_1 \hat{S}^z \sin(\omega_{rf} t)$  serves as the driving source for the dynamics of local spin state.

The spin dynamics is characterized by the temporal evolution of the reduced density matrix,  $\rho(t) \equiv \langle \rho_{\text{T}}(t) \rangle_{\text{res}}$ , where  $\rho_{\text{T}}(t)$  is the total density matrix. By utilizing the cumulant expansion of  $\rho_{\text{T}}(t)$  in the  $H'_{\text{int}}$ -interaction picture and the Born approximation  $\rho_{\text{T}}(t) \approx \rho_{\text{res}} \otimes \rho(t)$  [36], we obtain the following quantum master equation,

$$\dot{\rho}(t) = -i[H'_{\text{Zeeman}} + H_{\text{Drive}}(t), \rho(t)] + R(t). \quad (4)$$

Here, the commutator describes the Larmor precession of the local spin, and  $R(t)$  encapsulates the dissipation processes that involve the non-Markovian memory kernel  $\langle H'_{\text{int}}(t) H'_{\text{int}}(\tau) \rangle_{\text{res}}$ , which leads to the relaxation of local spin state. In the following, we neglect  $R(t)$  because of the weak spin-reservoir couplings [36]. Equation (4) with  $R(t) = 0$  formally recovers the dynamical theory of conventional ESR [30]. By performing the Laplace transform of Eq. (4) and presuming the initial state of the local spin is in isolated equilibrium,  $\rho(0) = \rho_{\text{eq}} = e^{-\beta H'_{\text{spin}}} / \text{tr}(e^{-\beta H'_{\text{spin}}})$ , we obtain the frequency-resolved reduced density matrix for a given driving frequency  $\omega_{rf}$ ,  $\tilde{\rho}(\omega + i\eta; \omega_{rf}) = \int_0^\infty dt e^{i(\omega+i\eta)t} \rho(t)$  [36].

The STM-ESR spectrum is measured as  $\tilde{I}(\omega_{rf}) = \lim_{t_f \rightarrow \infty} \frac{1}{t_f} \int_0^{t_f} dt I(t)$  by varying  $\omega_{rf}$ , where  $I(t) = -2 \text{Im}\{\text{tr}(H_{ts} \rho_{\text{T}})\}$ . By utilizing the cumulant expansion of  $\rho_{\text{T}}$  [36], we attain the following analytic formula,

$$\begin{aligned}
\tilde{I}(\omega_{rf}) &= iC \text{tr} \left[ H_{\text{spin}} \bar{S}^z \tilde{U}(i\eta) (\underline{S}^z - 1) \eta \tilde{\rho}(i\eta; \omega_{rf}) \right]_{\eta \rightarrow 0^+} \\
&= C \sin \theta \tilde{\mathbf{S}}(\omega_{rf}) \cdot \mathbf{e}_\perp. \quad (5)
\end{aligned}$$

Here, we define  $\bar{O} * \equiv [\hat{O}, *]$ ,  $\underline{O} * \equiv \{\hat{O}, *\}$ ,  $\tilde{U}(\omega) = i(\omega - \bar{H}_{\text{spin}})^{-1}$ , and  $\tilde{\mathbf{S}}(\omega_{rf}) = \text{tr}\{\hat{\mathbf{S}} \eta \tilde{\rho}(i\eta; \omega_{rf})\}_{\eta \rightarrow 0^+}$ .  $\mathbf{e}_\perp$  is a unit vector perpendicular to  $\mathbf{B}_{\text{ext}}$  within the plane spanned by  $\mathbf{B}_{\text{ext}}$  and  $B_{\text{tip}}^{\text{eff}} \hat{\mathbf{z}}$ , where the direction of  $\mathbf{B}_{\text{ext}}$  is arbitrary. The prefactor  $C$  is given by

$$C = \frac{\chi \Gamma_s \Gamma_t}{2\pi^2} \int \frac{D_t(\tilde{\omega}) D_s(\omega)}{(\omega - \epsilon)^2} [f_\beta(\tilde{\omega}) - f_\beta(\omega)] d\omega, \quad (6)$$

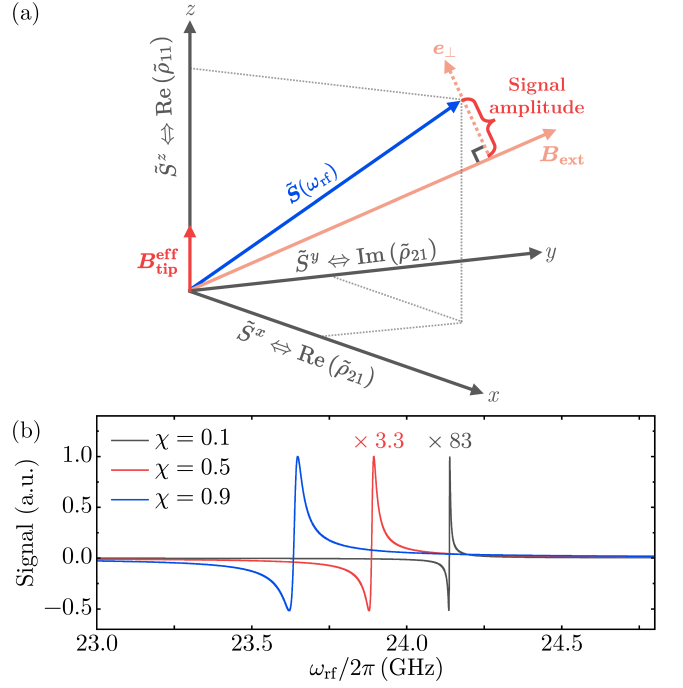


FIG. 4. (a) Geometric interpretation of the STM-ESR signal. (b) STM-ESR spectra of a single adatom of  $S = 1/2$  given by Eq. (5) at different  $\chi$  values, with signals normalized to the same amplitude. Adopted parameters are:  $|\mathbf{B}_{\text{ext}}| = 0.81$  T,  $\theta = 5^\circ$ ,  $\epsilon = -6$  meV,  $\Gamma_s = 0.2$  meV,  $\Gamma_t = 0.05$  meV,  $V_{dc} = V_{rf} = 0.4$  mV, and  $T = 1.2$  K.

with  $\tilde{\omega} = \omega + V_{dc}$ .

We now use the presented analytic theory to clarify the origin of the signal and decipher the essential features displayed in Fig. 2. Firstly, Eqs. (5) and (6) reveal that the STM-ESR signal arises from the net electron flow pumped by the Larmor precession of the local spin. These equations also reveal the circumstances under which the signal vanishes: a spin-unpolarized tip ( $\chi = 0$ ), alignment of  $\mathbf{B}_{\text{ext}}$  with  $\hat{\mathbf{z}}$  ( $\theta = 0$  or  $180^\circ$ ), or when  $V_{dc} = 0$ . Secondly, both  $\omega_L$  and  $\tilde{I}(\omega_{rf})$  are trigonometric functions of  $\theta$ . As evident in Fig. 2(b), our analytic theory accurately reproduces the  $\theta$ -dependence of the peak position and amplitude observed in numerical simulations. Thirdly, as shown in Fig. 2(c), the exponential decay of the signal with increasing temperature is accounted for by the Boltzmann factor in  $\rho_{\text{eq}}$ , while the nonlinear relationship between the signal and  $V_{rf}$  is explained by the amplification of  $\tilde{\mathbf{S}}(\omega_{rf})$  through  $B_{\text{tip}}^{\text{eff}}$ , along with the effects of high-order dissipation processes.

Interestingly, the analytic expression in Eq. (5) offers a geometric perspective on interpreting the STM-ESR signal. As illustrated in Fig. 4(a),  $\tilde{\mathbf{S}}(\omega_{rf})$  represents the time-averaged local spin moment influenced by the applied alternating voltage. Within the Kondo model, the spin dynamics can be fully characterized by three elements of the reduced density matrix:  $\text{Re}(\tilde{\rho}_{21})$ ,  $\text{Im}(\tilde{\rho}_{21})$  and  $\text{Re}(\tilde{\rho}_{11})$ . These elements correspond one-to-one to

the  $x$ ,  $y$ , and  $z$  components of  $\tilde{\mathbf{S}}$ , respectively. The signal amplitude is determined by the magnitude of the vector projection of  $\tilde{\mathbf{S}}$  onto  $\mathbf{e}_\perp$ . Specifically, when there is no applied alternating voltage,  $\tilde{\mathbf{S}} = \text{tr}(\tilde{\mathbf{S}}\rho_{\text{eq}})$  lies in the direction of  $\mathbf{B}_{\text{ext}}$ , resulting in zero signal.

To further explore the impact of the effective magnetic field  $B_{\text{tip}}^{\text{eff}}(t)$ , Fig. 4(b) depicts the evolution of the STM-ESR spectra given by Eq. (5) with varying  $\chi$  that measures the extent of tip spin-polarization. The spectra exhibit a Fano-like lineshape centered around the resonance frequency  $\omega_{\text{rf}} = \omega_L$ . It is noteworthy that both  $B_0$  and  $B_1$  vary linearly with  $\chi$ . The former causes a shift of the resonance center, while the latter results in substantial amplification of the signal and broadening of the resonance profile. These observations are consistent with experimental findings [14, 18].

The quantum master equation represented by Eq. (4) and the analytic expression encapsulated in Eq. (5) together form a comprehensive theoretical framework for STM-ESR of an individual spin system. This theory uncovers the underlying mechanism for spin dynamics to generate the ESR signal by the applied voltage at the STM tip, while it does not preclude the presence of synergistic effects from other sources [14, 21, 33]. Extending this theory to scenarios involving multiple adatoms or molecules is straightforward, which can be achieved by replacing the spin operator in Eq. (5) with that of the magnetic center directly coupled to the tip.

*Conclusion.* In summary, our numerical simulations of STM-ESR spectra for both a single hydrogenated Ti adatom and a hydrogenated Ti dimer accurately reproduce a wide array of important features observed in experiments. This validates both our modeling of the STM junction and our treatment of the bias voltage. Furthermore, our analytic theory reveals that the STM-ESR signal originates from the net electron flow pumped by the Larmor precession of the local spin. In terms of the mechanism and theory developed in this paper, the effective magnetic field  $B_{\text{tip}}^{\text{eff}}(t)$ , generated by the oscillation of the electrochemical potential of the spin-polarized tip, serves as the driving source for spin dynamics. The theoretical insights presented in this paper establish a solid foundation for designing innovative atomic-scale platforms with promising implications for on-demand spin sensing and manipulation.

## ACKNOWLEDGMENTS

The support from the National Natural Science Foundation of China (Grant Nos. 22203083 and 22393910), Innovation Program for Quantum Science and Technology (Grant No. 2021ZD0303305), and Strategic Priority Research Program of the Chinese Academy of Sciences (Grant No. XDB0450101) is gratefully acknowledged. The authors thank Xu Ding and Jian Cao for fruitful discussions.

- 
- [1] I. G. Rau, S. Baumann, S. Rusponi, F. Donati, S. Stepanow, L. Gragnaniello, J. Dreiser, C. Piamonteze, F. Nolting, S. Gangopadhyay, O. R. Albertini, R. M. Macfarlane, C. P. Lutz, B. A. Jones, P. Gambardella, A. J. Heinrich, and H. Brune, *Science* **344**, 988 (2014).
  - [2] E. Moreno-Pineda and W. Wernsdorfer, *Nat. Rev. Phys.* **3**, 645 (2021).
  - [3] A. J. Heinrich, W. D. Oliver, L. M. K. Vandersypen, A. Ardavan, R. Sessoli, D. Loss, A. B. Jayich, J. Fernández-Rossier, A. Laucht, and A. Morello, *Nat. Nanotechnol.* **16**, 1318 (2021).
  - [4] L. Bogani and W. Wernsdorfer, *Nat. Mater.* **7**, 179 (2008).
  - [5] E. Coronado, *Nat. Rev. Mater.* **5**, 87 (2020).
  - [6] E. Moreno-Pineda and W. Wernsdorfer, *Nat. Rev. Phys.* **3**, 645 (2021).
  - [7] T. Choi, W. Paul, S. Rolf-Pissarczyk, A. J. Macdonald, F. D. Natterer, K. Yang, P. Willke, C. P. Lutz, and A. J. Heinrich, *Nat. Nanotechnol.* **12**, 420 (2017).
  - [8] X. Zhang, C. Wolf, Y. Wang, H. Aubin, T. Bilgeri, P. Willke, A. J. Heinrich, and T. Choi, *Nat. Chem.* **14**, 59 (2022).
  - [9] F. D. Natterer, K. Yang, W. Paul, P. Willke, T. Choi, T. Greber, A. J. Heinrich, and C. P. Lutz, *Nature* **543**, 226 (2017).
  - [10] A. Singha, P. Willke, T. Bilgeri, X. Zhang, H. Brune, F. Donati, A. J. Heinrich, and T. Choi, *Nature Commun.* **12**, 4179 (2021).
  - [11] Y. Chen, Y. Bae, and A. J. Heinrich, *Adv. Mater.* **35**, 2107534 (2022).
  - [12] L. Bi, K. Liang, G. Czap, H. Wang, K. Yang, and S. Li, *Prog. Surf. Sci.* **98**, 100696 (2023).
  - [13] S. Loth, M. Etzkorn, C. P. Lutz, D. M. Eigler, and A. J. Heinrich, *Science* **329**, 1628 (2010).
  - [14] S. Baumann, W. Paul, T. Choi, C. P. Lutz, A. Ardavan, and A. J. Heinrich, *Science* **350**, 417 (2015).
  - [15] W. Paul, K. Yang, S. Baumann, N. Romming, T. Choi, C. P. Lutz, and A. J. Heinrich, *Nat. Phys.* **13**, 403 (2017).
  - [16] K. Yang, Y. Bae, W. Paul, F. D. Natterer, P. Willke, J. L. Lado, A. Ferrón, T. Choi, J. Fernández-Rossier, A. J. Heinrich, and C. P. Lutz, *Phys. Rev. Lett.* **119**, 227206 (2017).
  - [17] Y. Bae, K. Yang, P. Willke, T. Choi, A. J. Heinrich, and C. P. Lutz, *Sci. Adv.* **4**, eaau4159 (2018).
  - [18] P. Willke, W. Paul, F. D. Natterer, K. Yang, Y. Bae, T. Choi, J. Fernández-Rossier, A. J. Heinrich, and C. P. Lutz, *Sci. Adv.* **4**, eaq1543 (2018).
  - [19] P. Willke, A. Singha, X. Zhang, T. Esat, C. P. Lutz, A. J. Heinrich, and T. Choi, *Nano Lett.* **19**, 8201 (2019).
  - [20] K. Yang, W. Paul, F. D. Natterer, J. L. Lado, Y. Bae, P. Willke, T. Choi, A. Ferrón, J. Fernández-Rossier, A. J. Heinrich, and C. P. Lutz, *Phys. Rev. Lett.* **122**, 227203 (2019).
  - [21] T. S. Seifert, S. Kovarik, D. M. Juraschek, N. A. Spaldin,

- P. Gambardella, and S. Stepanow, *Sci. Adv.* **6**, eabc5511 (2020).
- [22] K. Yang, S.-H. Phark, Y. Bae, T. Esat, P. Willke, A. Ardavan, A. J. Heinrich, and C. P. Lutz, *Nat. Commun.* **12**, 1 (2021).
- [23] P. Willke, T. Bilgeri, X. Zhang, Y. Wang, C. Wolf, H. Aubin, A. Heinrich, and T. Choi, *ACS Nano* **15**, 17959 (2021).
- [24] P. Kot, M. Ismail, R. Drost, J. Siebrecht, H. Huang, and C. R. Ast, *Nat. Commun.* **14**, 1 (2023).
- [25] K. Yang, W. Paul, S.-H. Phark, P. Willke, Y. Bae, T. Choi, T. Esat, A. Ardavan, A. J. Heinrich, and C. P. Lutz, *Science* **366**, 509 (2019).
- [26] L. M. Veldman, L. Farinacci, R. Rejali, R. Broekhoven, J. Gobeil, D. Coffey, M. Ternes, and A. F. Otte, *Science* **372**, 964 (2021).
- [27] Y. Wang, Y. Chen, H. T. Bui, C. Wolf, M. Haze, C. Mier, J. Kim, D.-J. Choi, C. P. Lutz, Y. Bae, S.-h. Phark, and A. J. Heinrich, *Science* **382**, 87 (2023).
- [28] F. Delgado and J. Fernández-Rossier, *Prog. Surf. Sci.* **92**, 40 (2017).
- [29] F. Delgado and N. Lorente, *Prog. Surf. Sci.* **96**, 100625 (2021).
- [30] J. A. Weil and J. R. Bolton, *Electron Paramagnetic Resonance: Elementary Theory and Practical Applications* (Wiley, New York, 2007).
- [31] S. Müllegger, E. Rauls, U. Gerstmann, S. Tebi, G. Serrano, S. Wiespointner-Baumgarthuber, W. G. Schmidt, and R. Koch, *Phys. Rev. B* **92**, 220418(R) (2015).
- [32] A. M. Shakirov, A. N. Rubtsov, and P. Ribeiro, *Phys. Rev. B* **99**, 054434 (2019).
- [33] J. L. Lado, A. Ferrón, and J. Fernández-Rossier, *Phys. Rev. B* **96**, 205420 (2017).
- [34] J. Reina Gálvez, C. Wolf, F. Delgado, and N. Lorente, *Phys. Rev. B* **100**, 035411 (2019).
- [35] J. Reina-Gálvez, C. Wolf, and N. Lorente, *Phys. Rev. B* **107**, 235404 (2023).
- [36] See Supplemental Material at xxx for more details about the derivations..
- [37] J. R. Schrieffer and P. A. Wolff, *Phys. Rev.* **149**, 491 (1966).
- [38] Y. Tanimura and R. Kubo, *J. Phys. Soc. Jpn.* **58**, 101 (1989).
- [39] J. Jin, X. Zheng, and Y. Yan, *J. Chem. Phys.* **128**, 234703 (2008).
- [40] Z. H. Li, N. H. Tong, X. Zheng, D. Hou, J. H. Wei, J. Hu, and Y. J. Yan, *Phys. Rev. Lett.* **109**, 266403 (2012).
- [41] L. Ye, X. Wang, D. Hou, R.-X. Xu, X. Zheng, and Y. Yan, *WIREs Comput. Mol. Sci.* **6**, 608 (2016).
- [42] D. Zhang, L. Zuo, L. Ye, Z.-H. Chen, Y. Wang, R.-X. Xu, X. Zheng, and Y. Yan, *J. Chem. Phys.* **158**, 014106 (2023).
- [43] D. Zhang, L. Ye, J. Cao, Y. Wang, R.-X. Xu, X. Zheng, and Y. Yan, arXiv:2401.01715.
- [44] J. Kim, W. J. Jang, T. H. Bui, D.-J. Choi, C. Wolf, F. Delgado, Y. Chen, D. Krylov, S. Lee, S. Yoon, C. P. Lutz, A. J. Heinrich, and Y. Bae, *Phys. Rev. B* **104**, 174408 (2021).
- [45] J. Hwang, D. Krylov, R. Elbertse, S. Yoon, T. Ahn, J. Oh, L. Fang, W.-J. Jang, F. H. Cho, A. J. Heinrich, and Y. Bae, *Rev. Sci. Instrum.* **93**, 093703 (2022).